Energy-based Descriptors for Photo-Catalytically Active Metal-Organic Frameworks Discovery

Maria Fumanal*[1,2], Gloria Capano[1], Senja Barthel,[1,3] Berend Smit[1], Ivano Tavernelli*[2]

[1]Laboratory of Molecular Simulation, Institut des Sciences et Ingénierie Chimiques, Valais, Ecole Polytechnique Fédérale de Lausanne (EPFL), Rue de l'Industrie 17, CH-1951, Sion, Switzerland

[2]IBM Research Zurich, Säumerstrasse 4, 8803 Rüschlikon, Switzerland

[3]Department of Mathematics, Vrije Universiteit Amsterdam, De Boelelaan 1081, 1081 HV Amsterdam, The Netherlands

*maria.fumanal@epfl.ch, *ITA@zurich.ibm.com

Abstract

Metal-organic frameworks (MOFs) consist of metal nodes that are connected by organic linkers. They are thus highly chemically tunable materials given the broad range of potential linkers and nodes that can be chosen for their synthesis. Their tunability has recently sparked interest for the development of new MOF photo-catalysts for energy-related applications such as hydrogen (H_2) evolution and CO_2 reduction. The sheer amount of potentially synthesizable MOFs requires to define descriptors that allow to predict their performance with this aim. Herein we propose a systematic computational protocol to determine two energy-based descriptors that are directly related to the performance of a MOF as a photocatalyst. These descriptors assess the UV-vis light absorption capability and the band energy alignment with respect to redox processes and/or co-catalysts energy levels. High-throughput screening based on accurate computations of these features is envisioned to aid the discovery of new photoactive systems.

Introduction

Metal-organic frameworks (MOFs)[1] are crystalline materials consisting in metal clusters that are connected by organic linkers and are potentially porous. They are of interest for many applications due to their often high accessible surface areas. Among porous materials, MOFs have been shown to be promising materials for several applications such as gas storage,[2] gas separation,[3] catalysis[4,5] and sensing[6], due to their structural tunability, adjustable topology framework and chemical functionality.[7,8,9] These characteristics have recently been used for the development of efficient photocatalysts in order to address solar-driven chemical reactions such as hydrogen (H_2) evolution and CO_2 reduction.[10,11,12,13,14] The usage of MOFs for photocatalysis may overcome the main drawbacks of traditional TiO_2 and CdS photocatalysts. For example, TiO_2 has poor visible light absorption, while CdS has poor photostability. In MOFs we might be able to design materials with improved photocatalytic performance by means of strategic selection of light-responsive ligands and reductive metal ions such as Ti(IV) and Zr(IV).[15] For instance, remarkable H_2 production has been reported for different photocatalytic systems based on visible-light active MOFs such as MIL-125-NH_2[10,11] or the recently reported ZSTU- family.[16]

The modular nature of MOFs causes an almost unlimited number of hypothetical structures, which makes the traditional trial and error strategies to find materials of interest unfeasible. This explains the popularity of computational screenings of MOFs to tentatively predict target properties and to guide future efforts in synthesis. Previous high-throughput screening studies of MOFs have been developed to characterize their geometrical features, such as the pore size distribution and accessible surface area, while Grand Canonical Monte Carlo (GCMC) and Molecular Dynamics (MD) simulations are used to

compute and screen their target gas adsorption performance.[17,18,19,20,21,22] More recently, a high-throughput scheme for heterogeneous catalysis screening of MOFs was reported.[23] These and other studies rely on the generation of large databases of MOFs, experimental or hypothetical. These efforts have produced a vast library of MOFs for which photo-catalytical activity has not been tested, neither their potential has been evaluated. Screening the databased for the photo-catalytical activity will identify materials that are promising photocatalysts.

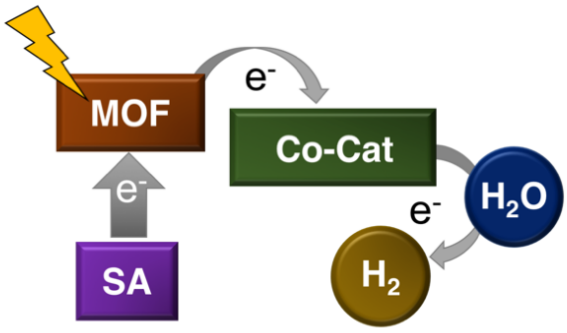

Figure 1. Scheme of the photo-catalytical process including MOF, co-catalyst (Co-Cat) and sacrificial agent (SA) for H_2 production.

A typical scheme of a photo-catalytical system with MOFs includes a co-catalyst and a sacrificial agent as depicted in Figure 1. The photo-catalytical process can be summarized in three main steps: (1) the electron-hole generation within the MOF by means of solar-light absorption, (2) the electron transfer to the co-catalyst and the MOF recovery via the sacrificial agent oxidation and (3) the catalytical reaction, for instance hydrogen H_2 production. In this context, a screening aiming at the detection of photocatalytic MOFs must make a pragmatic differentiation between (i) the energetic requirements that a MOF must fulfill to potentially be a photocatalyst and (ii) the electronic features that will make it highly efficient in its catalytic purpose, that is, the electronic features that determine its performance and stability. The first step determines the actual UV-vis and redox capabilities of the MOF in a given photocatalytic system, while the second step analyses desired properties for high efficiency, such as the exciton lifetime and electron photoconductivity. This two-level distinction is important to first identify potentially photo-catalytically active MOFs by searching for the energetic requirements, and only then evaluate the performance of the identified materials in a second step. This strategy is motivated by the fact that long-lived electron-hole pairs and high electron mobility will only provide a photo-catalytical response in the presence of visible-light if both the absorption and the thermodynamic energy of the photoelectron is appropriate.

To evaluate the UV-vis capabilities of medium-large metalorganic complexes, low-energy absorption spectra calculations can be easily obtained from Density Functional Theory (DFT)[24,25,26] calculations and its Time-Dependent extension within the Linear-Response formalism (LR-TDDFT).[27,28,29] However LR-TDDFT calculations are rarely applied for MOFs crystals[30] due to their usually large size and cluster models are used instead.[31,32] As another simplification, light absorption properties of periodic insulating or semiconductor systems have been traditionally associated with their electronic band gap. Nevertheless, it is still important to distinguish between the electronic band gap and the optical gap.[33] While the electronic band gap is a ground state property associated with an excitation energy in which the electron-hole interaction is not taken into account, the optical gap describes the lowest neutral excitation of the system including excitonic effects. To anticipate the low-lying absorption energies of molecular-like systems such as MOFs, explicit calculations of excitation energies and optical spectra with excitonic features should be considered.[34] Unfortunately, these calculations are computationally expensive and cannot be applied in a high-throughput manner for periodic systems, thus estimations from the electronic band gap are required.

Similarly, the photo-reductive capabilities of a periodic system to produce H_2 can be estimated from the energy of its conduction band (CB), obtained with reference to the vacuum potential value. The latter is commonly obtained by means of artificially introducing a vacuum space in between bulk layers.[35] However, there are two problems that hinder the usage of this approach to MOFs: the lack of knowledge about the surface cut and the high computational cost of enlarging the unit cell of an already large porous material. To find a practical solution, Walsh and

coworkers proposed to estimate the vacuum potential energy of porous MOFs by the value of the electrostatic potential energy at the center of the largest pore of the framework,[36] thus providing a reference scale of the electronic levels. It is expected that the discovery of photo-catalytically active MOFs will highly benefit from high-throughput computations designed to screen these two target descriptors.

In this work, we propose a computational scheme to evaluate two energy-based property-descriptors of MOFs that are directly related to their ability to act as photocatalysts and we apply it for a test-set of MOFs extracted from the Cambridge Structural Database (CSD).[37] The first descriptor assess the UV-visible absorption capability and the second descriptor determines the photo-redox potential and MOF/co-catalyst band energy alignment, provided the electronic energy levels of the later. Analyzing our test-set we found that several of the systems for which we predict UV-vis absorption are confirmed to show UV-vis absorption experimentally. This supports the reliability of our procedure. In addition, one particular promising system for photo-catalytical water splitting was identified. Our procedure provides a cost-efficient method to screen large MOF databases in a high-throughput manner to accelerate the discovery of high performance photocatalytic systems.

Methods

Datasets Construction

Two datasets were constructed in this work from the CSD MOF subset reported in 2017.[37] The first dataset (labeled **DS1**) contains orthorhombic Zn MOFs with unit cell volume up to 1000 Å^3, which results in 132 distinct crystalline structures. The CSD reference codes with the cell parameters and chemical composition are provided in Table S1 of SI. The second dataset (**DS2**) contains porous Zn or Cd MOFs with unit cell volume between 7000 and 8000 Å^3 and pore diameters between 5 and 13 Å^3 as determined by the program Zeo++[38]. A complete list of the 73 parsed Zn and Cd MOFs is provided in Table S2 of SI including the CSD reference codes, the cell parameters and the chemical composition.

Computational details

Fix-cell geometry optimizations were initially performed for **DS1** and **DS2** crystal structures under periodic boundary conditions after a careful examination of the presence of disorder and/or the need of adding missing hydrogens. The optimizations were performed using Quantum Espresso code[39] version 6.3. with the SSSP precision pseudopotential library.[40] The wave-function and charge-density cutoffs used are converged values with respect to phonon frequencies, pressure, cohesive energies and band structure calculations. The PBE[41] functional with Grimme D3 dispersion[42] correction and a Γ-point sampling of the Brillouin zone was used. PBE single point calculations were performed on the optimized structures at two k-points equally spaced in each direction of the reciprocal lattice.

A subset of the **DS1** optimized structures were further optimized using PBE functional and Grimme D2 dispersion[43] correction at Γ with the CPMD package[44,45] version 4.1. (Grimme D3 is not available in this version). Trouiller-Martins norm-conserving pseudopotentials[46] were used with a plane wave cutoff of 90 Ry for the orbitals and of 360 Ry for the density. Within the same setup, TDDFT calculations were performed with PBE and PBE0[47,48] functionals at the **DS1** re-optimized structures. For a subset of the **DS2** optimized structures, PBE0 ground state calculations were performed with the CPK2 code version 5.1.[49] at the Γ k-point using the Goedecker-Teter-Hutter pseudopotentials[50] with a density cutoff of 450 Ry and DZVP-MOLOPT basis set for non-metal atoms and TZVP-MOLOPT basis set for Zn/Cd atoms.[51] The auxiliary Density Matrix Method (ADMM) was used in order to reduce the computational cost, the auxiliary basis set pFIT3 (3 gaussian exponents per valence orbital, includes polarization d-functions) was used for non-metal atoms and cFIT11 (contracted, 4 s, 3 p, and 3 d shells and 1 f shell in total) for Zn/Cd atoms.

Electronic Chemical Potentials

Following the procedure previously reported by Walsh and coworkers[36], the electrostatic potential average in the pore of the **DS2** optimized structures was taken in

place of the vacuum level. However, we found that the structural complexity of the **DS2** test-set makes the electrostatic potential at the geometrical center of the pore an often inadequate choice for the electrostatic potential evaluation. That motivated us to implement an automated search for the value with the smallest variance within the MOF pore to most appropriately represent the reference level. This was included in a modified version of the already available MacroDensity package[52] (see Section S1 of ESI). Then, the Kohn-Sham energy levels ε_{KS} are aligned relative to this potential (Φ_{av}) as $\varepsilon_{KS}^{absolute} = \varepsilon_{KS} - \Phi_{av}$. The energy of the highest occupied level is taken as the ionization potential (*IP*). The electron affinity (*EA*) is calculated from the difference between the *IP* and the computed band gap E_g ($EA = IP - E_g$).

Results

The Results are discussed in two main sections. In **Section 1** we present the computational screening protocol to address the UV-vis and photo-redox properties of the selected **DS1** and **DS2** MOFs. In **Section 2**, the outcomes of the test screening are presented. The MOFs that are predicted to be photoactive are discussed and the results for those of our systems that have been experimentally studied are validated by comparing them to the experimentally obtained results. Finally, the computed IP/EA map of **DS2** MOFs is used to predict band energy alignment synergies with respect to some prototype H_2O/H_2 co-catalysts.

Section 1. Screening procedure for UV-vis light absorption and redox properties of MOFs

The scheme to evaluate and predict UV-visible absorption and photo-redox capabilities of MOFs materials is shown in Figure 2. In the following, we start by addressing the evaluation of the band gap and the lowest excitation energy with DFT methods.

Band gap. Electronic structure calculations of periodic crystals are easily accessible with DFT by applying the Bloch's theorem to the Kohn-Sham equations.[53] Within periodic DFT, integrals in real space are replaced by integrals over the Brillouin zone (BZ) in reciprocal space, which are discretized in the so-called k-point mesh. An appropriate choice of the k-point sampling is crucial to obtain reliable results and needs to be carefully converged. The optimal number of k-points usually depends on the size of the unit cell, systematically decreasing for bigger unit cells. This is because the BZ decreases in the reciprocal space with increasing unit cell sizes. In this context, it is a common strategy to use only one single k-point (called Γ) at the center of the BZ for big unit cells when possible to reduce the computational cost. This is usually the case for MOFs characterized with big pores and large unit cells, but still a statistical analysis for different size data-sets has not been reported.

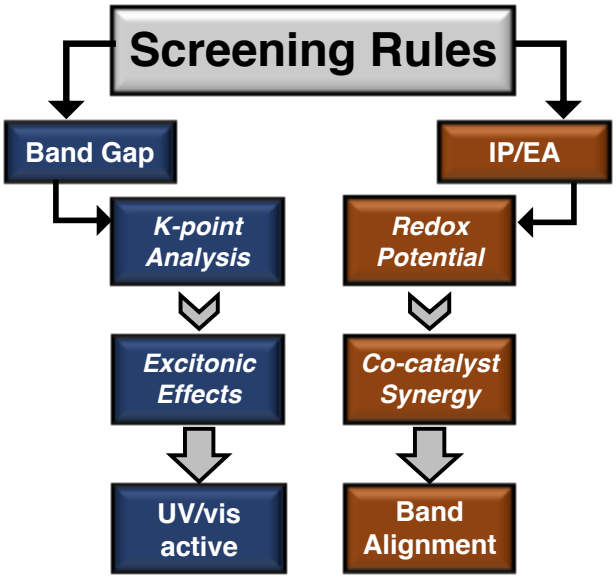

Figure 2. Schematic protocol designed to evaluate the UV-visible absorption capabilities and the photo-oxidant (or photo-reductive) properties of a given material, herein applied for MOFs

Γ-point and extended 2x2x2 k-point sampling was used to evaluate the electronic band gap of **DS1** and **DS2** structures. The computed band gaps obtained for **DS1** range from 0.5 to 5 eV. The error at Γ-point (ΔE_k) ranges from 0.0 to 2.0 eV and does not correlate with the band gap value (ΔE_k of ~1 eV can be found in MOFs with band gap of either 1.5 eV or 3.5 eV). The statistical analysis indicates that of the 132 cases, ~20% show a correction of >0.25 eV, while ~10% had a correction of more than 0.55 eV (Section S2 of SI). Performing the same analysis on 45 selected **DS2** structures shows that the computed band gap ranges from 1.5 eV to 4.0 eV and ΔE_k is zero or negligible (<0.1 eV) in all cases. Small ΔE_k in the case of the **DS2**

structures is ascribed to their large unit cell volumes (between 7000-8000 Å^3). In contrast, the relatively small volume of **DS1** (< 1000 Å^3) results in significant errors in 20% of the cases. We performed an analysis of the dependence of ΔE_k with the unit cell volume and with the maximum ratio between the a,b,c unit cell parameters, however no direct correlations were found (see Section S2 in SI). These examples show that a careful examination of the band gap convergence with respect to the k-point sampling is required for those particular cases that have small unit cells and large ratios between cell parameters. In our further analysis we excluded the 28 **DS1** structures with > 0.25 eV band gap error at Γ.

Excitation Energies. As mentioned in the introduction, explicit calculations of excitation energies and optical spectra have to be considered to predict low-lying absorption energies. But since these calculations cannot be performed in a high-throughput manner on periodic systems given their high computational cost, estimations obtained from the electronic band gap are needed. It is known that the local density approximation (LDA) or generalized gradient approximation (GGA) functionals that are used for cost-effective calculations of electronic band gaps, are underestimating the electronic band gap of insulators and semiconductors systematically.[54] Consequently, large effort has been undertaken in order to compute accurate band gaps of solids from DFT band structure calculations.[55,56,57] Among different strategies such as *GW* perturbation theory[55] or Hubbard-corrected DFT+*U*[58], hybrid schemes containing an admixture of nonlocal exact exchange have been shown to significantly improve the description of the electronic bang gap for a variety of materials.[56,57] In the following, we aim at predicting the absorption properties of MOFs by stablishing linear correlations between the generalized gradient approximation (GGA)-Perdew–Berke–Enzerhof (PBE) and the hybrid-PBE0 functional. This allows us to correct the results obtained from the cheaper PBE band gap calculations to estimate the more accurate but more costly hybrid-PBE0 functional results. For that we performed calculations with both functionals for selected **DS1** structures including LR-TDDFT evaluations of their low-lying excited energies. The results obtained were then used to optimize linear correlation functions between the computed bang gaps and the S_1 excited energies.

We found that Γ-point sampling provides adequate estimations for 104 structures of the 132 **DS1** set. Of the 104 structures, 36 structures (35%) show a PBE band gap value below 3.2 eV, energy associated with the upper limit of the visible light spectrum (380 nm). Given that GGA is well-known for underestimating band gaps, systems with higher values (band gap > 3.2 eV) were discarded as potential candidates for UV-vis absorption. Hence, PBE0 calculations were consequently performed for the remaining 36 systems.

To get some insights into the excitonic effects, the low-lying excited state energies were computed at PBE and PBE0 level by LR-TDDFT calculations with periodic boundary conditions. Correlations between the computed band gap and the lowest S_1 excited energies are shown in Figures 3b and 3c, respectively. It can be seen that PBE TDDFT calculations do not account for excitonic effects, that is, the electronic band gap and the computed S_1 energy coincide. In contrast, PBE0 results display a systematic reduction of about ~1.0±0.5 eV from the bang gap to the S_1 energy, which is ascribed to the exciton binding energy. The absence of excitonic effects in semilocal GGA-PBE functionals is due to the long-range behavior not being correctly captured by the exchange kernel. Hybrid exchange functionals replace a portion of the semilocal exchange energy with the exact exchange energy, which in periodic insulators has the non-local behavior necessary for the formation of excitons. However, the resulting unscreened electron–hole interaction may lead to an over-binding of the excitons.[33] The direct correlation between the computed PBE band gap and the PBE0 S_1 energies is shown in Figure 3a (raw data is given in Table S7). Based on the root mean square value R^2 obtained from linear regression (0.73), one can anticipate that the prediction based on the band gaps will be subject to a significant error (±0.5 eV). A systematic shift of 0.85 eV will therefore be used to estimate the lowest absorption edge.

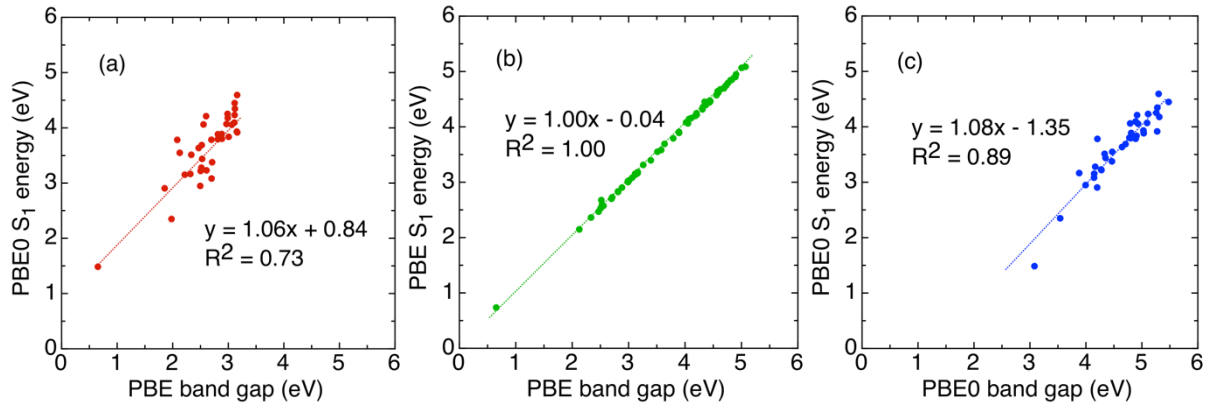

Figure 3. Correlations between (a) the PBE band gap and PBE0 S_1 energy, (b) the PBE band gap and PBE S_1 energy and (c) PBE0 band gap and PBE0 S_1 energy. Linear regresion fittings are provided. Raw data is given in Table S6 of ESI.

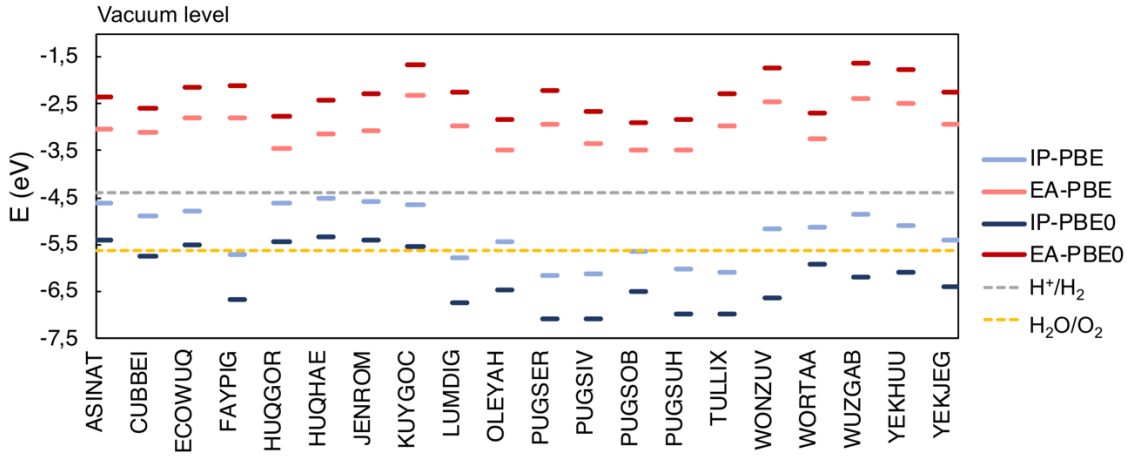

Figure 4. Computed ionization potential (blue) and electron affinity (red) of 20 selected **DS2** structures with respect to the vacuum level which is chosen as the electrostatic potential inside the pore of the MOF. PBE and PBE0 values are provided, as well as the reference H^+/H_2 and H_2O/O_2 potentials. Raw data is collected in Table S8 of ESI.

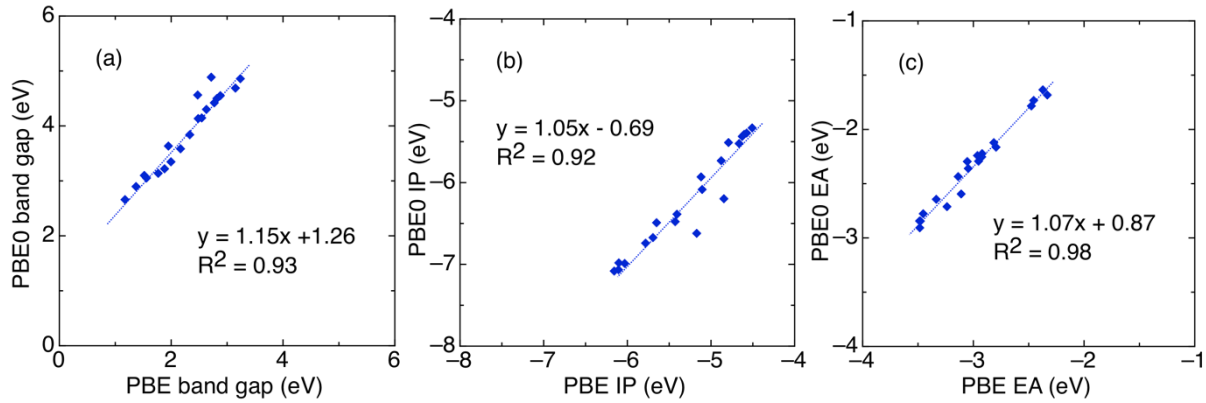

Figure 5. Correlation between PBE and PBE0 obtained values of (a) band gap (b) ionization potential IP and (c) electron affinity EA of the 20 selected **DS2** structures. Linear regression fittings are provided. IP and EA values correspond to the highest occupied and lowest empty energy levels. Raw data is collected in Table S8 of ESI.

Band energy alignment. Whereas the electronic band gap of a given MOF determines whether it will absorb in the visible range of light, its redox properties are controlled by the absolute energies of its conduction and valence band-edges. These energies must be placed on an absolute scale within a band energy alignment diagram to consider their redox-capabilities with respect to a given reaction or their redox-synergy with a particular co-catalyst,.[36,59,60,61] The valence and conduction band edges in solids can be represented by the energy of the highest occupied and lowest empty energy levels, respectively, when aligned relative to a vacuum reference potential. After this alignment, they can be associated with the ionization potential (IP) and electron affinity (EA) of the material, respectively, the difference of which corresponds to the electronic band gap (see Methods).

So far, our previous evaluation of the electronic band gap did not provide information about the position of the band-edges and thus, cannot be used to predict any photo-catalytical activity. To this aim, we computed the electrostatic potential at a representative point inside the largest pore of the **DS2** structures (see Methods) and used this value as the vacuum potential.[36] The IP and EA were then obtained as the difference between the highest occupied and lowest empty energy levels as explained above. The PBE and PBE0 results obtained for 20 selected **DS2** structures are represented in Figure 4 (raw data is given in Table S8 of SI). Remarkably, it shows that the predicted redox-capabilities can strongly depend on the level of theory used (PBE or PBE0) and thus, accurate references are needed.

Linear regressions between the PBE and PBE0 computed IP and EA values were optimized in order to stablish empirical rules to estimate the valence and conduction band-edges, respectively. The correlations obtained (Figure 5) provide R^2 values above 0.9 and predict an average shift of -0.7 eV between the PBE and PBE0 computed IP, and of +0.9 eV in the case of EA. The concerned negative and positive shift of the IP and EA values, respectively, that appear when exact exchange is included, is in agreement with the expected opening of the underestimated PBE band gap. However, it is worth emphasizing that the correction does not equally apply to the valence and conduction bands, being systematically larger for the later. Applying the proposed shifts to the PBE computed values results in a mean absolute error below <0.1 eV with respect to the PBE0 calculations.

The resulting computational protocol to evaluate the potential of MOFs as photocatalysts is summarized in the following steps:

1) Validation of the Γ point calculations for band gap and electronic structure analysis and corrections from k-point sampling.
2) UV-vis absorption edge estimation by applying a systematic shift of 0.85 eV to the PBE band gap, derived from comparison with PBE0.
3) For porous MOFs, alignment of the PBE levels with respect to vacuum and shift of the VB and CB values by -0.7 and +0.9 eV, respectively.
4) Build appropriate band energy diagrams to screen a target reaction or co-catalyst synergy.

Section 2. Screening of the UV-vis absorption, IP/EA map and co-catalyst band alignment.

In this section, we discuss the computational screening of the MOFs in the sets **DS1** and **DS2** by applying the screening protocol developed in the previous section.

On the basis of the computed excited energies, we find that 11 **DS1** structures potentially absorb below 3.5 eV. Relevant information about these materials is collected in Table 1, including their CSD reference codes and their main chemical compositions. From the 11 systems, 6 are hybrid inorganic-organic nanostructures consisting of ZnSe or ZnTe layers that are connected by diamine molecules as spacers. Notably, these composite materials were designed with the aim of combining the semiconducting functionality of the inorganic constituent with the low weight and high processability of the organic component. In particular, they offer significant variations onto the optical properties of their inorganic frameworks and provide considerably blue-shifted absorption-edges starting at 3.3 eV in the case of ZnTe composites[66] and at 3.9 eV in the case of ZnSe[70]. Our computed values overstabilize their lowest absorption edge by ~0.6 eV, while predicting the correct trend

between the two sets of ZnTe and ZnSe compounds. Similarly, photoluminescence studies were undertaken on material **2** on Table 1, for which a moderately blue-green fluorescence was measured upon excitation at 325 nm.[67] This system contains a well-known photo-active azobenzene group characterized by two relatively intense bands in the UV spectrum at 220-240 and 320-360 nm, and weak absorption in the visible >400 nm,[62] in agreement with our estimation. Optical properties of the other 4 screened compounds were not reported in their original publications. However, naphthalene compounds, such as **9** and **11** on Table 1, are well known for their wide application in the fluorescence field, being characterized by an absorption band-edge at ~350 nm,[63] and indole derivatives are characterized by optical absorption spectra starting above 300 nm, as has been predicted for system **6**.[64]

Despite the large diversity of the chemical composition of the studied materials, our screening based on PBE0 calculations of the S_1 energies was able to identify a set of systems for which low-energy absorption is experimentally expected. Remarkably, it is found that their characteristic UV-vis absorption bands can either originate in ZnTe/ZnSe inorganic layers, or are localized in optically active ligands such as azobenzene/naphthalene. This highlights the complexity of assessing empirical models to accurately predict their optical band gap and points to the need of *ab initio* calculations. However, we demonstrated that reasonable estimations can be made from cost-effective methods such as PBE by establishing direct correlations with accurate methods, such as hybrid PBE0 used herein. Future high-throughput screenings applied on MOFs are envisioned with this purpose.

PBE-corrected IP and EA values for all **DS2** structures are plotted in Figure 6 along with their corresponding electronic band gaps. The computed EA values indicate that all systems will be energetically able to reduce H^+/H_2 upon excitation. This can be inferred from the conduction band edge being located above the H^+/H_2 redox potential in all cases. In contrast, the position of the valence band edge is found either above or below the redox potential that is needed to generate O_2. Only in the cases in which the EA and IP are predicted above the H^+/H_2 and below the H_2O/O_2 redox potentials, the system is potentially capable to cleaving water upon absorption of light.[65] If the valence band edge is above the H_2O/O_2 redox potential, a sacrificial agent becomes necessary to recover the neutral MOF provided that their redox-synergy is appropriate.

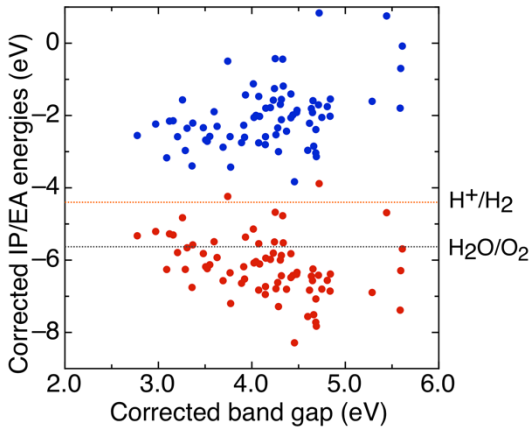

Figure 6. PBE-corrected IP (red) and EA (blue) energies of **DS2** structures mapped onto their PBE-corrected band gap values.

The IP and EA corrected energies spread over ~4.5 eV ranging from -4.0 to 0.5 eV for the EA, and from -4.0 to -8.5 eV for the IP. Now we retract our consideration to those structures whose corrected band gaps predict light absorption in the visible spectrum. This decision was made with the same screening procedure that is outlined above for **DS1**. Given that excitonic effects were not evaluated here, we tentatively consider a band gap energy threshold of 0.2 eV above the upper limit of the visible spectrum (3.2 eV). Among the 73 explored structures, 11 (15%) are identified as potentially absorbing in the visible range of light since they have corrected band gaps below 3.4 eV. Relevant information about the screened materials is collected in Table 2, including the CSD reference code and main chemical composition. The systems cover a wide range of properties from single-crystal transmetilation reactions reported for **1**, **2**, **4** and **5**,[74,76,77] to selective CO_2 capture for **8**.[80] Notably, UV-visible absorption has been experimentally reported for the systems **3**,[75] **7**,[79] **9**[81] and **11**[83] associated with charge-transfer or local π-π* excitations within the ligands, therefore validating our screening.

Table 1. The 11 MOFs from **DS1** that potentially absorb below 3.5 eV, with their computed (PBE0) and predicted (PBE-corrected: PBE-c) UV-vis absorption energies (eV) and wavelengths (nm). PBE-c is obtained by adding 0.85 eV to the PBE band gap. PBE0 S_1 energies are the reference values. The CSD reference codes and the chemical composition in terms of the metal cluster and the main ligand is also given.

	CSD ref	PBE-c (eV)	PBE0 S_1 (eV)	Abs. Diff. (eV)	PBE-c abs. (nm)	PBE0 abs. (eV)	Metal cluster	Main ligand
1	QOBHEU[66]	2.828	2.349	0.479	439	528	ZnTe	Ethylenediamine
2	QENFUL[67]	2.705	2.905	-0.200	458	427	ZnO_4N_2	Pyridyl-diaza-butadiene
3	QOBHEU01[66]	3.345	2.948	0.397	371	421	ZnTe	Ethylenediamine
4	QOBHIY[66]	3.549	3.082	0.467	349	402	ZnTe	Propanediamine
5	PYZNDT[68]	3.067	3.152	-0.085	404	393	ZnO_4N_1	Pyridine-dithionato
6	PUBGID[69]	3.167	3.165	0.002	391	392	ZnO_6	Indole-carboxylato
7	MICDUX[70]	3.352	3.219	0.133	370	385	ZnSe	Ethylenediamine
8	VAMWEM[71]	3.458	3.230	0.228	359	384	ZnSe	Butanediamine
9	IYEXEP[72]	3.366	3.279	0.087	368	378	ZnO_4	Naphtalene-dicarboxylato
10	MICFAF[70]	3.559	3.377	0.182	348	367	ZnSe	Propylenediamine
11	HERYOT[73]	3.379	3.438	-0.059	367	361	ZnO_6	naphtalene-tetracarboxylato

Table 2. The 11 MOFs from **DS2** that potentially absorb below 3.4 eV, with their computed PBE and PBE-corrected IP and EA values (in eV). PBE-corrected band gaps obtained as EA-IP are also given. The CSD reference codes and the chemical composition considering the constituent ligands is provided.

	CSD ref	PBE IP	PBE EA	BG	IP-0.7	EA+0.9	Main ligands
1	HUQGOR[74]	-4.627	-3.453	2.774	-5.327	-2.553	nitrilotribiphenyl-4-carboxylate ethene-1,2-diyldipyridine
2	HUQHAE[74]	-4.508	-3.137	2.971	-5.208	-2.237	nitrilotribiphenyl-4-carboxylate ethene-1,2-diyldipyridine
3[a]	DEVWOT[75]	-5.559	-4.070	3.089	-6.259	-3.170	1,2-bis(4,4′-bipyridinium)ethane 5-methylisophthalate
4	JENROM[76]	-4.574	-3.055	3.119	-5.274	-2.155	nitrilotribiphenyl-4-carboxylate 4,4'-bipyridine
5	ASINAT[77]	-4.604	-3.046	3.158	-5.304	-2.146	nitrilotribiphenyl-4-carboxylate di(pyridin-4-yl)-4H-1,2,4-triazol-4-amine
6	WARFAZ[78]	-5.091	-3.486	3.205	-5.791	-2.586	L-alanine naphthalene diimide 4,4′-bipyridine
7[b]	ZUCGAH[79]	-4.127	-2.468	3.258	-4.827	-1.568	benzyl substituted porphyrin
8	MUQSAU[80]	-5.557	-3.868	3.288	-6.257	-2.968	biphenyl-2,2',6,6'-tetracarboxylate ethene-1,2-diyldipyridine
9[c]	XEJJII[81]	-4.959	-3.253	3.307	-5.659	-2.353	furan-2,5-dicarboxylate (selenophene-2,5-diyl)dipyridine
10	VULWEF[82]	-6.055	-4.295	3.360	-6.755	-3.395	benzene-1,4-dicarboxylate (4-carboxyphenyl)-4,4′-bipyridinium
11[d]	CUBBEI[83]	-4.878	-3.110	3.368	-5.578	-2.210	curcumin

[a] Absorption in the visible has been reported for system **3** associated to a charge-transfer transition.
[b] System 7 corresponds to the porphyrin precursor used to synthesize a photo-redox catalyst including boron-dipyrromethene.
[c] UV-vis absorption of **9** is associated to local π-π* transitions of the aromatic rings in the framework.
[d] Curcumin is a yellow pigment characterized by an π-π* electronic transition that becomes blue-shifted upon metal-complexation.[84]

Knowing the valence- and conduction-band positions of the systems, energy-band diagrams can be constructed. These allows anticipating the direction of the photoinduced electron injection. One possible strategy is to combine photoactive MOFs with appropriate co-catalysts to boost the photocatalytic performance. For photocatalytic hydrogen H_2 production, representative examples of reduction co-catalysts that promote proton reduction in conjunction with MOFs are Ni_2P,[10] Pt[85] or MoS_2[86] nanoparticles. The band alignment synergies of these co-catalyst with the first five **DS2** MOFs from Table 2 are shown in Figure 7. Particularly promising is compound **3** (DEVWOT)[75] for which both the UV-vis and photo-

redox requirements for the water splitting photocatalytic purpose are fulfilled. This MOF was specifically designed to display low-energy charge transfer (CT) phenomena by means of π-staking interactions between electron-rich and electron-deficient units. In particular, UV-vis light excitation promotes CT from phenyl-carboxylate to bipyridine components (see Figure 8). The non-local character of the excitation could even improve the photocatalytic activity as it is associated with long exciton lifetimes.

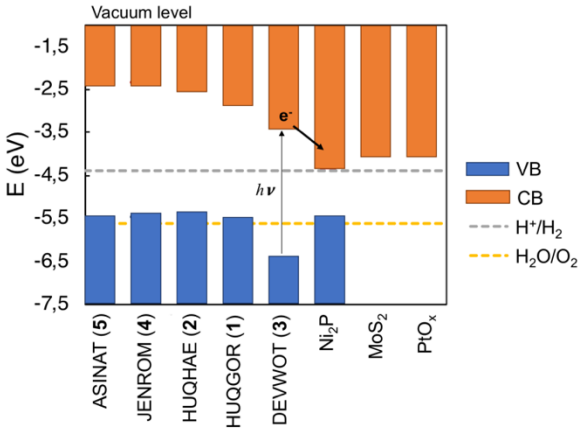

Figure 7. Diagram of the electronic energy levels computed in this work for selected **DS2** MOFs and values collected for representative co-catalysts.[10,85,86]

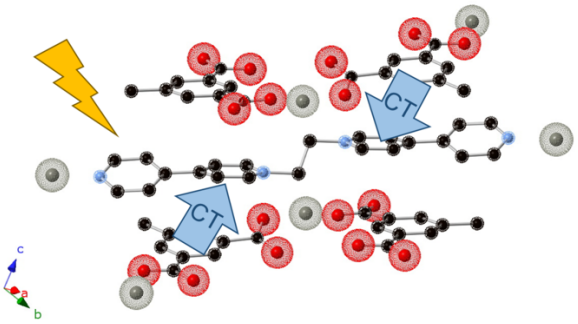

Figure 8. Schematic representation of photoinduced charge transfer (CT) between donor and acceptor units in MOF **3** of **DS2** (DEVWOT).[75]

Conclusions.

With the rapid increase of available crystallographic data of MOFs, the use of high-throughput computational screening has become a promising tool to aid the identification and characterization of materials with desired properties. Although any computationally accessible descriptor can be in principle included in a high-throughput screening process, its rapidness and feasibility are still requirements for a screening to become an efficient and valuable complementary approach to the experiments. This makes the design of cost-effective property-descriptors essential, as well as the determination of the error committed and its validation.

In this work, we propose a screening protocol to evaluate two energy-based descriptors that are directly related to the performance of MOFs as photocatalysts. These descriptors assess the UV-vis absorption capabilities and photo-redox properties based on DFT electronic structure calculations. Our results show that the first can be directly estimated from the PBE band gap considering a systematic shift of 0.85 eV that corrects the well-known overestimation of GGA functionals, as well as the inability of PBE to account for excitonic effects in solids. Furthermore, the absolute position of the conduction- and valence-bands is evaluated with respect to the electrostatic potential computed at a representative point inside the pore of the MOF structure, which is taken as the vacuum potential. Comparing PBE and PBE0 calculations shows a systematic shift of -0.7 for the valence band and of +0.9 eV for the conduction band.

Performing the screening on our selected test-sets of MOFs allowed to validate the strategy and provided a set of photoactive MOF that have been synthesised but not studied with respect to their photo-catalytical activity. In particular, MOF structure **3** of **DS2** (DEVWOT) displays suitable UV-vis light absorption and desirable absolute VB and CB energies for water splitting, as well as promising excited state features for long lived excitonic lifetimes. Future analysis is envisioned to include this and other performance descriptors associated with enhanced photo-catalytical activity.

Supporting information.

Section S1. Electronic Chemical Potential. **Section S2.** Band gap k-points analysis. **Table S1.** DS1 MOF structures. **Table S2.** DS2 MOF structures. **Table S3 and S4.** DS1 structures k-point analysis. **Table S5.** DS2 structures k-point analysis. **Table S6 and S7.**

Band gap and absorption of DS1 structures. **Table S8 and S9.** IP and EA of DS2 structures.

Acknowledgements.

This work has been supported by EPFL and the National Centre of Competence in Research (NCCR) Materials Revolution: Computational Design and Discovery of Novel Materials (MARVEL) of the Swiss National Science Foundation (SNSF). Calculations were performed at the EPFL High Performance Computer Center SCITAS.

References.

[1] Ferey, G. Hybrid porous solids: past, present, future. *Chem. Soc. Rev.* **2008**, *37*, 191−214.

[2] Mason, J. A.; Oktawiec, J.; Taylor, M. K.; Hudson, M. R.; Rodriguez, J.; Bachman, J. E.; Gonzalez, M. I.; Cervellino, A.; Guagliardi, A.; Brown, C. M.; Llewellyn, P. L.; Masciocchi, N.; Long, J. R. Methane storage in flexible metal−organic frameworks with intrinsic thermal management. *Nature* **2015**, *527*, 357−361.

[3] Li, J.-R.; Kuppler, R. J.; Zhou, H.-C. Selective gas adsorption and separation in metal-organic frameworks. *Chem. Soc. Rev.* **2009**, *38*, 1477−1504.

[4] Liu, J.; Chen, L.; Cui, H.; Zhang, J.; Zhang, L.; Su, C.-Y. Applications of metal-organic frameworks in heterogeneous supra- molecular catalysis. *Chem. Soc. Rev.* **2014**, *43*, 6011−6061.

[5] Corma, A.; García, H.; Llabreś i Xamena, F. X. , Engineering Metal Organic Frameworks for Heterogeneous Catalysis. *Chem. Rev.* **2010**, *110*, 4606−4655.

[6] Lustig, W. P.; Mukherjee, S.; Rudd, N. D.; Desai, A. V.; Li, J.; Ghosh, S. K. Metal-organic Frameworks: Functional Luminescent and Photonic Materials for Sensing Applications. *Chem. Soc. Rev.* **2017**, *46*, 3242−3285.

[7] Zhou, H.-C; Long, J. R.; Yaghi, O. M. Introduction to Metal–Organic Frameworks. *Chem. Rev.* **2012**, *112*, 673-674.

[8] Schoedel, A.; Li, M.; Li, D.; O'Keeffe, M.; Yaghi, O. M. Structures of Metal–Organic Frameworks with Rod Secondary Building Units. *Chem. Rev.* **2016**, *116*, 12466-12535.

[9] Valizadeh, B.; Nguyen, T. N.; Stylianou, K. C. Shape engineering of metal–organic frameworks *Polyhedron*, **2018**, *145*, 1-15.

[10] Kampouri, S. ; Nguyen, T. N.; Ireland, C. P.; Valizadeh, B.; Ebrahim, F. M.; Capano, G.; Ongari, D.; Mace, A.; Guijarro, N.; Sivula, K.; Sienkiewicz, A.; Forró, L.; Smit, B.; Stylianou K. C. Photocatalytic hydrogen generation from a visible-light responsive metal–organic framework system: the impact of nickel phosphide nanoparticles. *J. Mater. Chem. A*, **2018**, *6*, 2476-2481.

[11] Kampouri, S. ; Nguyen, T. N.; Spodaryk, M.; Palgrave, R. G.; Züttel, A.; Smit, B.; Stylianou, K. C.; Concurrent Photocatalytic Hydrogen Generation and Dye Degradation Using MIL-125-NH2 under Visible Light Irradiation. *Adv. Funct. Mat.* **2018**, *28*, 1806368.

[12] Dhakshinamoorthy, A.; Li, Z.; Garcia, H. Catalysis and photocatalysis by metal organic frameworks. *Chem. Soc. Rev.*, **2018**, *47*, 8134-8172.

[13] Chen, L.; Wang, Y.; Yu, F.; Shen, X.; Duan, C. A simple strategy for engineering heterostructures of Au nanoparticle-loaded metal–organic framework nanosheets to achieve plasmon-enhanced photocatalytic CO2 conversion under visible light. *J. Mater. Chem. A*, **2019**, *7*, 11355-11361.

[14] Syzgantseva, M. A.; Ireland, C. P.; Ebrahim, F. M.; Smit, B.; Syzgantseva O. A. Metal Substitution as the Method of Modifying Electronic Structure of Metal–Organic Frameworks. *J. Am. Chem. Soc*., **2019**, *141*, 6271-6278.

[15] Yuan, S.; Qin, J.-S.; Xu, H.-Q.; Su, J.; Rossi, D.; Chen, Y.; Zhang, L.; Lollar, C.; Wang, Q.; Jiang, H.-L.; Son, D. H.; Xu, H.; Huang, Z.; Zou, X.; Zhou, H.-C. [Ti8Zr2O12(COO)16] Cluster: An Ideal Inorganic Building Unit for Photoactive Metal−Organic Frameworks. *ACS Cent. Sci.* **2018**, *4*, 105−111.

[16] Li, C.; Xu, H.; Gao, J.; Du, W.; Shangguan, L.; Zhang, X.; Lin, R.-B.; Wu, H.; Zhou, W.; Liu, X.; Yao J.; Chen, B. Tunable titanium metal–organic frameworks with infinite 1D Ti–O rods for efficient visible-light- driven photocatalytic H2 evolution *J. Mater. Chem. A*, **2019**, *7*, 11928-11933.

[17] Wilmer, C. E.; Leaf, M.; Lee, C. Y.; Farha, O. K.; Hauser, B. G.; Hupp, J. T.; Snurr, R.Q. Large-scale screening of hypothetical metal– organic frameworks. *Nat. Chem.* **2012**, *4*, 83–89.

[18] Bernini, M.C.; Fairen-Jimenez, D.; Pasinetti, M.; Ramirez-Pastor, A. J.; Snurr, R.Q. Screening of bio-compatible metal-organic frameworks as potential drug carriers using Monte Carlo simulations. *J. Mater. Chem. B* **2014**, *2*, 766–774.

[19] Simon, C. M.; Kim, J.; Gomez-Gualdron, D. A.; Camp, J. S.; Chung, Y. G.; Martin, R. L.; Mercado, R.; Deem, M.; Gunter, D.; Haranczyk, M.; Sholl, D. S. The materials genome in action: identifying the performance limits for methane storage. *Energy Environ. Sci.* **2015**, *8*, 1190– 1199.

[20] Colon, Y. J.; Fairen-Jimenez, D.; Wilmer, C. E.; Snurr, R.Q. High-throughput screening of porous crystalline materials for hydrogen storage capacity near room temperature. *J. Phys. Chem. C* **2014**, *118*, 5383–5389.

[21] Li, S.; Chung, Y. G.; Snurr, R. Q. High-Throughput Screening of Metal–Organic Frameworks for CO2 Capture in the Presence of Water. *Langmuir* **2016**, *32(40)*, 10368-10376.

[22] Avci, G.; Velioglu, S.; Keskin S. High-Throughput Screening of MOF Adsorbents and Membranes for H2 Purification and CO2 Capture *ACS Appl. Mater. Interfaces* **2018**, *10*, 33693−33706.

[23] Rosen, A. S.; Notestein, J. M.; Snurr, R. Q. Identifying Promising Metal–Organic Frameworks for Heterogeneous Catalysis Via High-Throughput Periodic Density Functional Theory *J. Comput. Chem.* **2019**, *40,* 1305–1318.

[24] Hohenberg, P.P.; Kohn, W. Inhomogeneous Electron Gas. *Phys. Rev.* **1964**, *136*, B864.

[25] Kohn, W.; Sham, L. J. Self-Consistent Equations Including Exchange and Correlation Effects. *Phys. Rev.* **1965**, *140*, A1133.

[26] Becke, D. Density-functional thermochemistry. III. The role of exact exchange. *J. Chem. Phys.* **1993**, *98*, 5648.

[27] Runge, E.; Gross, E. K. U. Density-Functional Theory for Time-Dependent Systems. *Phys. Rev. Lett.* **1984**, *52*, 997.

[28] Petersilka, M. ; Grossmann, U. J.; Gross, E. K. U. Excitation Energies from Time-Dependent Density-Functional Theory *Phys. Rev. Lett.* **1996**, *76*, 1212.

[29] Casida, M. E.; Huix-Rotlant, M. Progress in Time-Dependent Density-Functional Theory. *Annu. Rev. Phys. Chem.* **2012**, *63*, 287-323.

[30] Vrubel, I. I.; Senkevich, N. Y.; Khramenkova, E. V.; Polozkov, R. G.; Shelykh. I. A. Electronic Structure and Optical Response of Zn-Based Metal–Organic Frameworks. *Adv. Theory Simul.* **2018**, *1*, 1800049.

[31] Ji, M.; Lan, X.; Han, Z.; Hao, C.; Qiu, J. Luminescent Properties of Metal−Organic Framework MOF-5:Relativistic Time-Dependent Density Functional Theory Investigations, *Inorg. Chem.* **2012**, *51(22)*, 12389-12394.
[32] Wilbraham, L.; Coudert F.-X.; Ciofini, I. Modelling photophysical properties of metal–organic frameworks: a density functional theory based approach *Phys. Chem. Chem. Phys.*, **2016**, *18,* 25176—25182.
[33] Ullrich A. C.; Yang, Z.-h. Excitons in Time-Dependent Density-Functional Theory. *Top Curr Chem* **2016**, *368*, 185–218
[34] Wiktor, J.; Reshetnyak,I.; Strach,M.; Scarongella, M.; Buonsanti, R.; Pasquarello. A. Sizable Excitonic Effects Undermining the Photocatalytic Efficiency of β-$Cu_2V_2O_7$. *J. Phys. Chem. Lett.* **2018**, *9*, 5698−5703.
[35] Mamonova M. V.; Prudnikov V. V. Calculation of the electron work function at metal surfaces by a density functional method *Russ. Phys. J.*, **1998**, *41(12)*, 1174–1179.
[36] Butler, K. T.; Hendon, C. H.; Walsh A. Electronic Chemical Potentials of Porous Metal−Organic Frameworks *J. Am. Chem. Soc.* **2014**, *136*, 2703−2706.
[37] Moghadam, P. Z.; Li, A.; Wiggin, A. B.; Tao, A.; Maloney, A. G. P.; Wood, P. A.; Ward, S. C.; Fairen-Jimenez D. Development of a Cambridge Structural Database Subset: A Collection of Metal−Organic Frameworks for Past, Present, and Future *Chem. Mater.* **2017**, *29*, 2618−2625.
[38] Willems, T. F.; Rycroft, C. H.; Kazi, M.; Meza, J. C.; Haranczyk, M. Algorithms and tools for high-throughput geometry- based analysis of crystalline porous materials. *Microporous Mesoporous Mater.* **2012**, 149, 134-141.
[39] Giannozzi, P. et al. QUANTUM ESPRESSO: a modular and open-source software project for quantum simulations of materials. *J. Phys. Condens. Matter* **2009**, *21*, 395502.
[40] Standard solid-state pseudopotentials (SSSP); http://www.materialscloud.org/sssp/
[41] Perdew, J. P.; Burke K.; Ernzerhof, M. Generalized Gradient Approximation Made Simple, *Phys. Rev. Lett.*, **1996**, *77*, 3865.
[42] Grimme, S.; Antony, J.; Ehrlich, S.; Krieg H. A consistent and accurate ab initio parametrization of density functional dispersion correction (DFT-D) for the 94 elements H-Pu. *J. Chem. Phys* **2010,** *132*, 154104.
[43] Grimme, S. Semiempirical GGA-type density functional constructed with a long-range dispersion correction. *J. Comp. Chem.* **2006**, *27*, 1787-1799.
[44] Marx D.; Hutter, J. Mod. Methods Algorithms Quantum Chemistry, NIC, edited by J. Grotendorst (Forschungszentrum Jülich, 2000), Chap. 13, pp. 301–449.
[45] Andreoni W. Curioni, A. New advances in chemistry and materials science with CPMD and parallel computing. *Parallel Comput.* **2000,** *26*, 819-842.
[46] Troullier N., Martins, J.L., Efficient pseudopotentials for plane-wave calculations, *Phys. Rev. B* **1991**, *43*, 1993.
[47] Ernzerhof, M.; Scuseria, G. E., Assessment of the Perdew-Burke-Ernzerhof exchange-correlation functional, *J. Chem. Phys.*, **1999**, *110*, 5029-5036.
[48] Adamo C.; Barone, V. Toward reliable density functional methods without adjustable parameters: The PBE0 model, *J. Chem. Phys.,* **1999**, *110*, 6158-6169.
[49] Hutter, J.; Iannuzzi, M.; Schiffmann F.; VandeVondele, J. cp2k: atomistic simulations of condensed matter systems. *WIREs Comput. Mol. Sci.* **2014,** *4*, 15-25.
[50] Goedecker, S.; Teter, M.; Hutter, J. Separable dual-space Gaussian pseudopotentials. Phys. Rev. B 1996, 54, 1703.
[51] VandeVondele J.; Hutter, J. Gaussian basis sets for accurate calculations on molecular systems in gas and condensed phases *J. Chem. Phys.,* **2007**, *127*, 114105.
[52] https://github.com/WMD-group/MacroDensity
[53] Kratzer P.; Neugebauer, J. The Basics of Electronic Structure Theory for Periodic Systems, *Front. Chem.* **2019**, 7:106.
[54] Chan, M. K. Y.; Ceder, G. Efficient Band Gap Prediction for Solids. *Phys. Rev. Lett.* **2010**, *105*, 196403.
[55] Morales-García, A.; Valero, R.; Illas, F. An Empirical, yet Practical Way To Predict the Band Gap in Solids by Using Density Functional Band Structure Calculations, *J. Phys. Chem. C* **2017**, *121*, 18862−18866.
[56] Muscat, J.; Wander, A.; Harrison, N.M. On the prediction of band gaps from hybrid functional theory, *Chem. Phys. Lett.* **2001**, *34(21)*, 397-401.
[57] Perdew, J. P. ; Yang, W.; Burke, K.; Yang, Z.; Gross, E. K. U.; Scheffler, M.; Scuseria, G. E.; Henderson, T. M.; Zhang, I. Y.; Ruzsinszky, A.; Peng, H.; Sun, J.; Trushin, E.; GörlingA. Understanding band gaps of solids in generalized Kohn-Sham theory. *Proc. Natl. Acad. Sci. U. S. A.* **2017**, *114*, 2801−2806.
[58] Himmetoglu, B.; Floris, A.; de Gironcoli, S.; Cococcioni, M. Hubbard-Corrected DFT Energy Functionals: The LDA+U Description of Correlated Systems. *Int. J. Quantum Chem.* **2014**, *114*, 14−49.
[59] Walsh A.; Butler, K. T. Prediction of Electron Energies in Metal Oxides, *Acc. Chem. Res.* **2014**, *472*, 364-372.
[60] Walsh, A.; Butler, K. T.; Hendon, C. H.; Chemical principles for electroactive metal–organic frameworks, *MRS Bulletin*, **2016**, *41(11),* 870-876.
[61] Calbo, J.; Golomb M. J.; Walsh, A. Redox-active metal–organic frameworks for energy conversion and storage, *J. Mater. Chem. A*, **2019**, 7, 16571.
[62] Goreowen, P. H.; Wheeler, H. Absorption Spectra of Aromatic Azo and Related Compounds. III. Substituted Azobenzenes *J. Org. Chem.* **1961** *269* 3295-3298.
[63] Bincy, I. P.; Srinivasan, T.; Jaisankar, S. N.; Ramkumar V. Structure, growth and characterization of a new naphthalene family crystal for fluorescence and third order nonlinear optical applications *Solid State Sci* **2019**, *89*, 85-92.
[64] Lo, C.; Doucoure, B. I.; Aaron, J.-J.; Svoboda, J.; Kozmik, V.; Brochon, J.-C.; Henry, E.; Maurel, F.; Capochichi, M. Synthesis and spectral properties of new fluorescent alkoxy-substituted thieno[3,2-b]indole derivatives *Spectrochim. Acta Part A: Molecular and Biomolecular Spectroscopy*, **2014**, *120*, 47-54
[65] Grätzel, M. Photoelectrochemical cells, *Nature* **2001**, *414*, 338–344.
[66] Huang X.; Li, J. The First Covalent Organic-Inorganic Networks of Hybrid Chalcogenides: Structures That May Lead to a New Type of Quantum Wells *J. Am. Chem. Soc*. **2000**, *122*, 8789-8790.
[67] Zhang, G.; Yang, G.; Ma, J. S. Anion Control of the Self-Assembly of One-Dimensional Molecular Ladders vs Three-Dimensional Cross-like Arrays Based on a Bidentate Schiff Base Ligand, Cryst. Growth Des., 2006, 6, 1897-1902.
[68] Kiers, C.T.; Vos, A. The nature of the S-S bonds in different compounds. V. The crystal structure of ZnS2O4.pyridine. *Acta Crystallographica, Section B: Struct. Crystallogr. Cryst. Chem.,* **1978**, *34*, 1499-1504.
[69] Morzyk-Ociepa B. X-ray diffraction and vibrational spectroscopic studies of indolecarboxylic acids and their metal complexes Part VII. Indole-2-carboxylic acid and catena-poly[[diaquazinc(II)]-bis (m2-indole-2-carboxylato-O:O0)] *Vib. Spectrosc.* **2009**, *49*, 68–79.
[70] Huang, X.; Heulings, H. R. IV; Le, V.; Li, J. Inorganic-Organic Hybrid Composites Containing MQ (II-VI) Slabs: A New Class of Nanostructures with Strong Quantum Confinement and Periodic Arrangement, *Chem. Mater.* **2001**, *13*, 3754-3759.
[71] Xiaoying Huang, Jing Li, [ZnSe(dbn)1/2] and [ZnSe(hda)1/2]: Two new members of inorganic-organic hybrid semiconductor nanocomposites exhibiting a strong quantum confinement effect. *Materials Research Society, Symposium Proceedings,* **2002**, *728*, 17-22.

[72] Kongshaug K. O.; Fjellva, H. Organically pillared layered zinc hydroxides *J. Solid State Chem.* **2004**, *177*, 1852–1857

[73] Nielsen, R. K. B.; Kongshaug, K. O.; Fjellvåg H. Syntheses, crystal structures and thermal properties of 3D coordination polymers assembled from 1,4,5,8-naphthalenetetracarboxylic acid *Solid State Sci.* **2006**, *8*, 1237–1242.

[74] De, D.; Neogi, S.; Sañudo, E. C.; Bharadwaj, P. K. Single-Crystal to Single-Crystal Linker Substitution, Linker Place Exchange, and Transmetalation Reactions in Interpenetrated Pillared–Bilayer Zinc(II) Metal–Organic Frameworks *Chem.-A Eur. J.,* **2015**, *21*, 17422.

[75] Yang, X.-D.; Zhu, R.; Sun, L.; Guo, R.-Y. Zhang, J. Phototriggered Mechanical Movement in A Bipyridinium-based Coordination Polymer Powered by Electron Transfer *Inorg. Chem.* **2018**, *57(5),* 2724-2729.

[76] Qinghua, M. CSD Communication, 2017

[77] De, D.; Neogi, S.; Bharadwaj, P. K. Stoichiometry Controlled Structural Variation in Three-Dimensional Zn(II)–Frameworks: Single-Crystal to Single-Crystal Transmetalation and Selective CO2 Adsorption *Crystal Growth & Design* **2016**, *16(9),* 5238-5246.

[78] Boer, S. A.; Turner, D. R. A robust metallomacrocyclic motif for the formation interpenetrated coordination polymers *CrystEngComm*, **2017**, *19*, 2402.

[79] Lifschitz, A. M.; Young, R. M.; Mendez-Arroyo, J.; Stern, C. L.; McGuirk, C. M.; Wasielewski, M. R.; Mirkin, C. A. An allosteric photoredox catalyst inspired by photosynthetic machinery *Nat. Comm*., **2015**, *6*, 6541.

[80] Xu, Y.-L.; Gao, Q.; Zhao, M.; Zhang, H.-J.; Zhang, Y-H.; Chang, Z. Impact of the flexibility of pillar linkers on the structure and CO2 adsorption property of ‘‘pillar-layered’’ MOFs. *Chin. Chem. Lett*., **2017**, *28*, 55-59.

[81] Hua, C.; D’Alessandro, D. M.; Systematic Tuning of Zn(II) Frameworks with Furan, Thiophene, and Selenophene Dipyridyl and Dicarboxylate Ligands. *Crystal Growth and Design*, **2017**, *17*, 6262-6272.

[82] Higuchi, M.; Tanaka, D.; Horike, S.; Sakamoto, H.; Nakamura, K.; Takashima, Y.; Hijikata, Y.; Yanai, N.; Kim, J.; Kato, K.; Kubota, Y.; Takata, M.; Kitagawa, S. Porous Coordination Polymer with Pyridinium Cationic Surface, [Zn2(tpa)2(cpb)] *J. Am. Chem. Soc*., **2009**, *131,* 10336-10337.

[83] Su, H.; Sun, F.; Jia, J.; He, H.; Wang, A.; Zhu, G. A highly porous medical metal–organic framework constructed from bioactive curcumin. *Chem. Comm*., **2015**, *51*, 5774.

[84] Waranyoupalin, R.; Wongnawa, S.; Wongnawa, M.; Pakawatchai, C.; Panichayupakaranant, P.; Sherdshoopongse, P. Studies on complex formation between curcumin and Hg(II) ion by spectrophotometric method: A new approach to overcome peak overlap, *Cent. Eur. J. Chem*. **2009**, *7(3)*, 388.

[85] Horiuchi, Y.; Toyao, T.; Saito, M.; Mochizuki, K.; Iwata, M.; Higashimura, H.; Anpo, M.; Matsuoka, M. Visible-Light-Promoted Photocatalytic Hydrogen Production by Using an Amino-Functionalized Ti(IV) Metal−Organic Framework. *J. Phys. Chem C.* **2012**, *116*, 20848−20853.

[86] Nguyen, T. N.; Kampouri, S.; Valizadeh, B.; Luo, W.; Ongari, D.; Planes, O. M; Züttel, A.; Smit, B.; Stylianou, K. C. Photocatalytic Hydrogen Generation from a Visible-Light-Responsive Metal−Organic Framework System: Stability versus Activity of Molybdenum Sulfide Cocatalysts. *ACS Appl. Mater. Interfaces* **2018**, *10*, 30035−30039.